# Multishell structured magnetic nanocomposites carrying copolymer of pyrrole–thiophene for highly selective Au(III) recovery

Mingying Zhu,[a] Wei Zhang,[b] Yan Li,[a] Ligang Gai,[a]* Jianhua Zhou,[a] and Wanyong Ma[a]

[a]*Institute of Advanced Energy Materials and Chemistry, School of Chemistry and Pharmaceutical Engineering, Qilu University of Technology, Jinan 250353, People's Republic of China*

[b]*Dongying Entry-Exit Inspection and Quarantine Bureau, Dongying 257000, People's Republic of China*

*Corresponding author: E-mail: liganggai@qlu.edu.cn

## Table of Contents

**S1. Synthesis of $Fe_3O_4/SiO_2$, $Fe_3O_4/SiO_2$/PPy, and $Fe_3O_4/SiO_2$/PTh nanocomposites**

Before synthesis of $Fe_3O_4/SiO_2$ nanocomposite, $Fe_3O_4$ ferrofluid was first prepared through a chemical co-precipitation method.[1] Briefly, 8.94 mmol $FeCl_3 \cdot 6H_2O$, 5 mmol $FeSO_4 \cdot 7H_2O$, and 120 mL of distilled water were added into a three-neck flask with capacity of 250 mL. The mixture was bubbled with $N_2$, accompanying with agitation to form a clear solution. The reaction temperature was raised to 50 °C, followed by dropwise addition of 4 mL of concentrated $NH_3 \cdot H_2O$ (28 wt.%). Then, the mixture was heated at 85 °C for 1 h with constant stirring and $N_2$ bubbling, and allowed to cool to room temperature. After that, 2.5 mL of tetraethoxysilane were added into the mixture. The mixture was vigorously agitated at room temperature for 3 h. The precipitate was collected by applying a hand-held permanent magnet, washed with distilled water and ethanol several times, and finally dried in a vacuum oven.

For the synthesis of $Fe_3O_4/SiO_2$/PPy, 0.6 g of $Fe_3O_4/SiO_2$ powders, 50 mL of 0.05 mol $L^{-1}$ hydrochloric acid (HCl) solution, and 10 mg of sodium dodecyl sulfate were added into a three-mouth flask with capacity of 250 mL. The mixture was treated with ultrasound for 5 min, and

agitated at room temperature for 0.5 h. Then, the temperature of the mixture was decreased to 5 °C in an ice-bath. Subsequently, 0.9 mL of redistilled pyrrole was added into the mixture, followed by agitation for 1 h. After that, 20 mL of 0.97 mol $L^{-1}$ $FeCl_3$ aqueous solution was slowly added into the above mixture. The polymerization reaction was kept at 5 °C for 3 h with constant stirring and intermittent ultrasonication. The precipitate was separated by a hand-held magnet, washed with distilled water and ethanol several times, and collected by filtration. Finally, the resulting product was dried in a vacuum oven.

As for $Fe_3O_4/SiO_2$/PTh, 0.6 g of $Fe_3O_4/SiO_2$ powders, 60 mL of chloroform, and 10 mg of sodium dodecyl sulfate were added into a three-mouth flask with capacity of 250 mL, followed by ultrasonic treatment at room temperature for 10 min. Then, 1 mL of thiophene was added into the mixture. The mixture was vigorously stirred at room temperature for 1 h, followed by addition of 2.53 g of anhydrous $FeCl_3$. After vigorous agitation with intermittent ultrasonic treatment for 3.5 h, the mixture was separated with a hand-held magnet. The precipitate was washed with ethanol several times, collected by filtration, and finally dried in a vacuum oven.

## S2. Characterization of core–shell structured $Fe_3O_4/SiO_2$

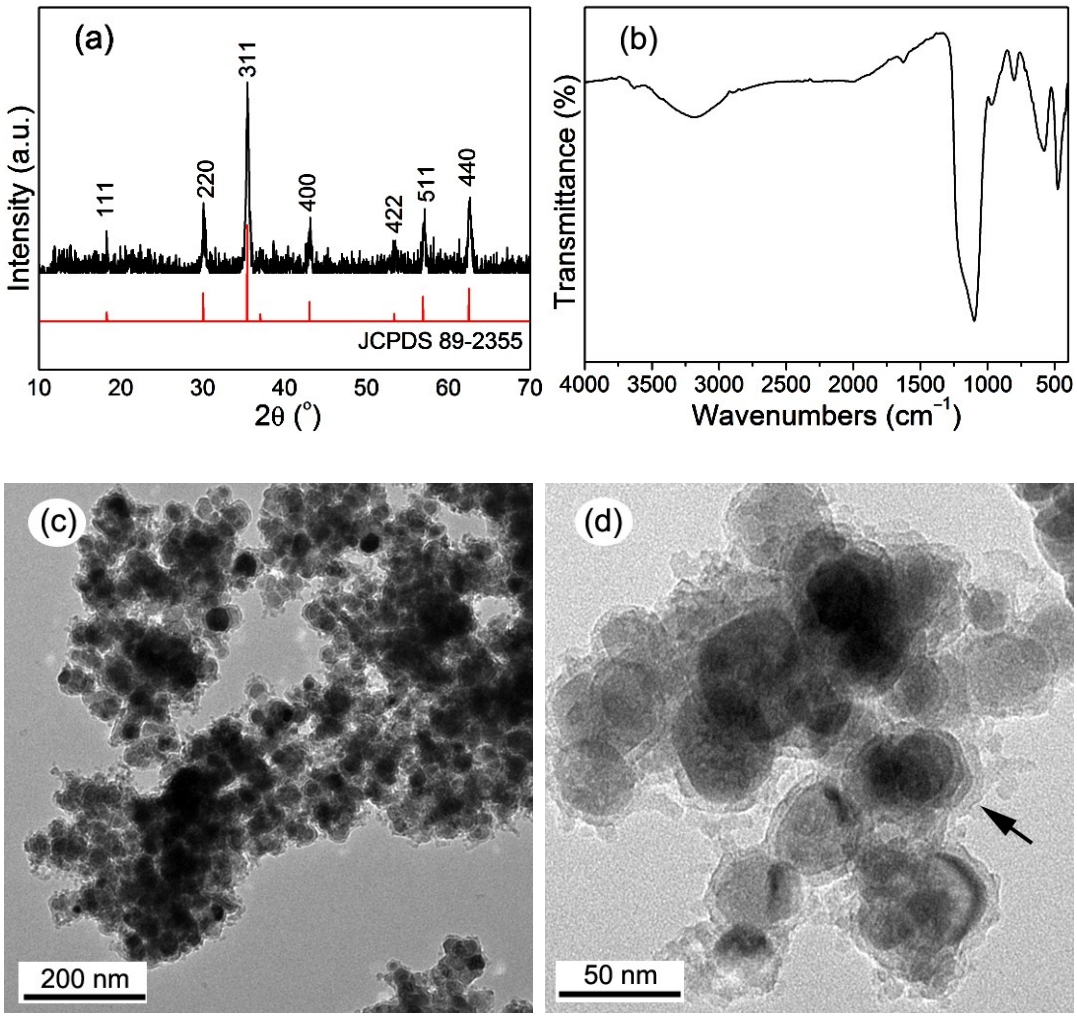


**Fig. S1** Characterization of $Fe_3O_4/SiO_2$: (a) XRD spectra; (b) FT-IR spectrum; (c,d) TEM image.

Fig. S1a shows the XRD pattern of $Fe_3O_4/SiO_2$. In view of the amorphous nature of silica coating, the diffraction peaks can be indexed to the (111), (220), (311), (400), (422), (511), and (440) planes of face-centered cubic $Fe_3O_4$ (JCPDS 89-2355). This result indicates that the magnetite phase is retained after silica coating. Using the data of (311), (511), and (440) planes, the mean size of $Fe_3O_4$ crystallites in $Fe_3O_4/SiO_2$ is estimated to be 25.2 nm, according to the Scherrer equation.

The silica shell of the magnetic composite can be confirmed by the FT-IR spectrum (Fig. S1b). The broad peak centered at 3200 $cm^{-1}$ are due to the stretching vibrations of O–H arising from silanols and surface adsorbed water. The strong and broad peak at 1097 $cm^{-1}$ and the small peak centered at 802 $cm^{-1}$ are attributed to the asymmetric and symmetric stretching vibrations of Si–O–Si in $SiO_2$.[2-5] The peaks centered at 967 and 474 $cm^{-1}$ correspond separately to the bending vibrations of SiO–H and SiO–Si.[5] The peak centered at 575 $cm^{-1}$ is attributed to the stretching vibration of Fe–O bond in $Fe_3O_4$.[2,3]

The morphology of $Fe_3O_4/SiO_2$ is reflected by the TEM images. Although the composite nanoparticles are aggregated due to magnetic dipolar interactions (Fig. S1c), the core–shell structure of the composite can be clearly discerned from the high-magnification TEM image (Fig. S1d). Because silica is amorphous with light contrast while magnetite is crystalline with dark contrast (Fig. S1a), the core–shell structured composite is in the form of silica-coated magnetite. In some cases, multiscaled silica shell occurs in the composite (the region indicated by an arrow in Fig. S1d), rendering shell thickness in the range of 5–18 nm. To estimate the weight percentage of silica in $Fe_3O_4/SiO_2$, sample powders were dissolved in a plastic bottle with hydrofluoric acid to form a clear solution. The solution was sampled and measured by the ICP–OES technique, giving a value of 33.8% for the weight percentage of silica in $Fe_3O_4/SiO_2$.

On the basis of sample characterizations, we conclude that: (1) the magnetite phase is retained after silica coating; (2) the magnetic silica exhibits a core–shell structure in the form of silica-coated

magnetite with shell thickness of 5–18 nm; (3) the weight percentage of silica in the magnetic composite is estimated to be 33.8% through the ICP–OES technique.

## S3. Theoretical calculations

**Table S1** Theoretical calculation results related to pyrrole, thiophene, and their oligomers.

| molecular formula* | orbital energy (eV) | | | energy (a.u.) | | Difference in energy |
|---|---|---|---|---|---|---|
| | HOMO | LUMO | Δ*E* | molecule | cation radical | kJ mol$^{-1}$ |
| $C_4H_4S$ | -6.33459 | -0.20735 | 6.12724 | -553.0026285 | -552.6902656 | 820.1 |
| $C_4H_5N$ | -5.48395 | 1.38589 | 6.86984 | -210.1658907 | -209.879343 | 752.3 |
| SS | -5.47497 | -1.24738 | 4.22759 | -1104.8165369 | -1104.5556149 | 685.1 |
| SN | -5.03197 | -0.6743 | 4.35767 | -761.9822168 | -761.7352016 | 648.5 |
| NN | -4.65046 | 0.24763 | 4.89809 | -419.1479562 | -418.9137743 | 614.8 |
| $N_3$ | -4.30624 | -0.16681 | 4.13943 | -628.130651 | -627.9197031 | 553.8 |
| $N_4$ | -4.24392 | -0.29742 | 3.9465 | -837.115121 | -836.9156897 | 523.6 |
| $N_5$ | -4.14378 | -0.4343 | 3.70949 | -1046.0983794 | -1045.9070233 | 502.4 |
| $N_6$ | -4.08854 | -0.51158 | 3.57696 | -1255.0814111 | -1254.8958841 | 487.1 |
| $N_7$ | -4.048 | -0.57525 | 3.47274 | -1464.0646582 | -1463.883274 | 476.2 |
| $N_8$ | -4.01344 | -0.62995 | 3.38349 | -1673.0482929 | -1672.8697271 | 468.8 |
| $N_9$ | -3.99738 | -0.66015 | 3.33723 | -1882.0316191 | -1881.8555422 | 462.3 |
| $N_{10}$ | -3.9797 | -0.68546 | 3.29424 | -2091.0145674 | -2090.8407164 | 456.4 |
| SSS | -5.13701 | -1.68848 | 3.44853 | -1656.6316049 | -1656.3934095 | 625.4 |
| SNS | -4.81945 | -1.18887 | 3.63057 | -1313.7992866 | -1313.5705795 | 600.5 |
| NSS | -4.84421 | -1.36793 | 3.47628 | -1313.7973767 | -1313.5688162 | 600.1 |
| NNS | -4.55141 | -0.82125 | 3.73017 | -970.9652595 | -970.7456633 | 576.5 |
| NSN | -4.59087 | -0.94207 | 3.6488 | -970.9625648 | -970.7430634 | 576.3 |
| SSSS | -5.00884 | -1.87678 | 3.13206 | -2208.4469625 | -2208.2217468 | 591.3 |
| SNSS | -4.79686 | -1.5195 | 3.27737 | -1865.6152348 | -1865.396609 | 574.0 |
| NSSS | -4.80883 | -1.66753 | 3.14131 | -1865.6130436 | -1865.3949725 | 572.5 |
| SNNS | -4.59141 | -1.05717 | 3.53424 | -1522.7836657 | -1522.5714148 | 557.3 |
| NSNS | -4.62243 | -1.21935 | 3.40308 | -1522.7808483 | -1522.5689453 | 556.4 |
| NNSS | -4.59223 | -1.35487 | 3.23736 | -1522.7814687 | -1522.5698509 | 555.6 |
| NSSN | -4.64175 | -1.39868 | 3.24308 | -1522.7789774 | -1522.5675192 | 555.2 |
| NNNS | -4.40828 | -0.82642 | 3.58186 | -1179.9494621 | -1179.7438243 | 539.9 |
| NNSN | -4.44121 | -0.96764 | 3.47356 | -1179.9469435 | -1179.7415798 | 539.2 |

*N and S denote pyrrole ring and thiophene ring in the oligomers, respectively.

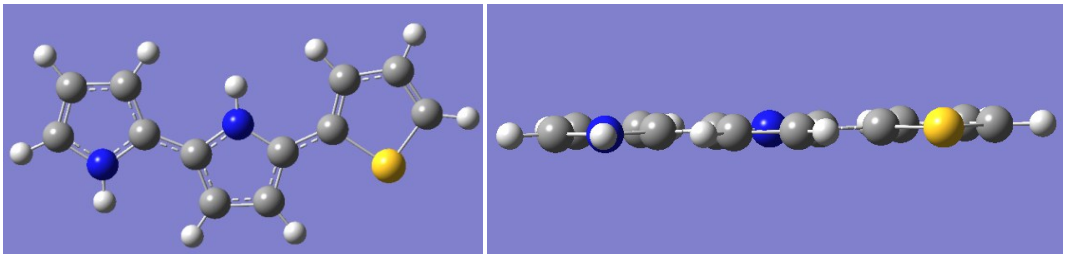

NNS

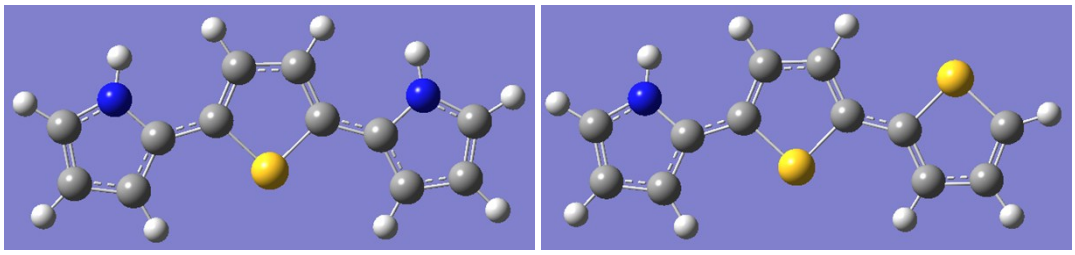

NSN NSS

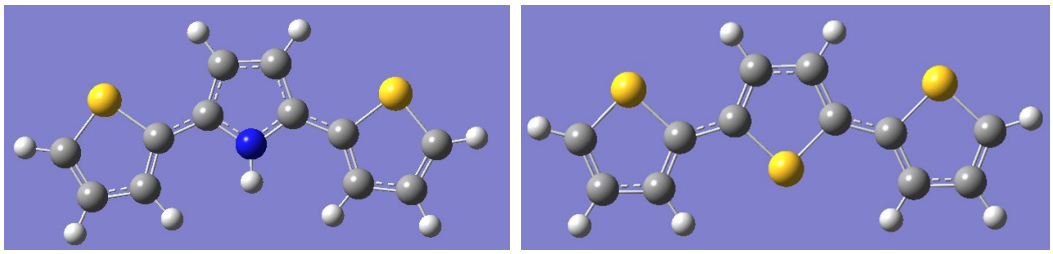

SNS SSS

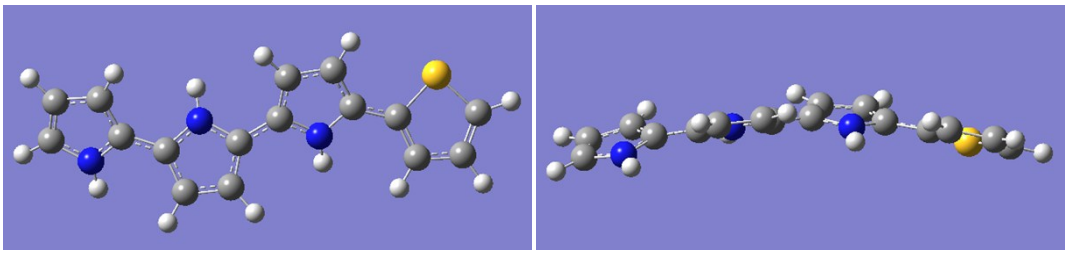

NNNS

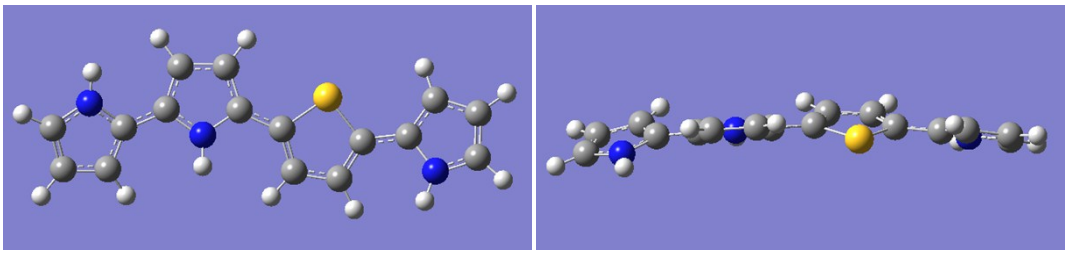

NNSN

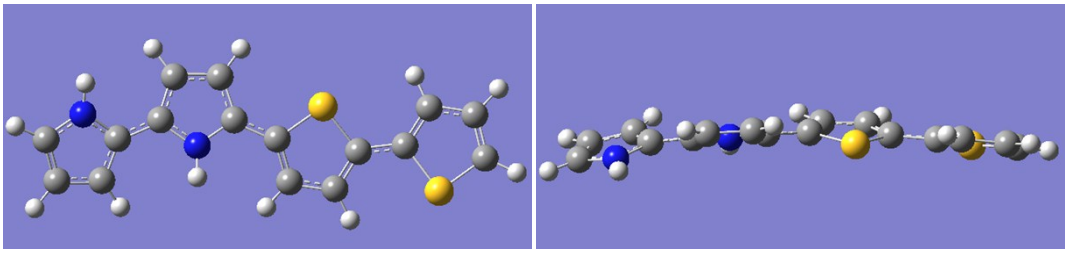

NNSS

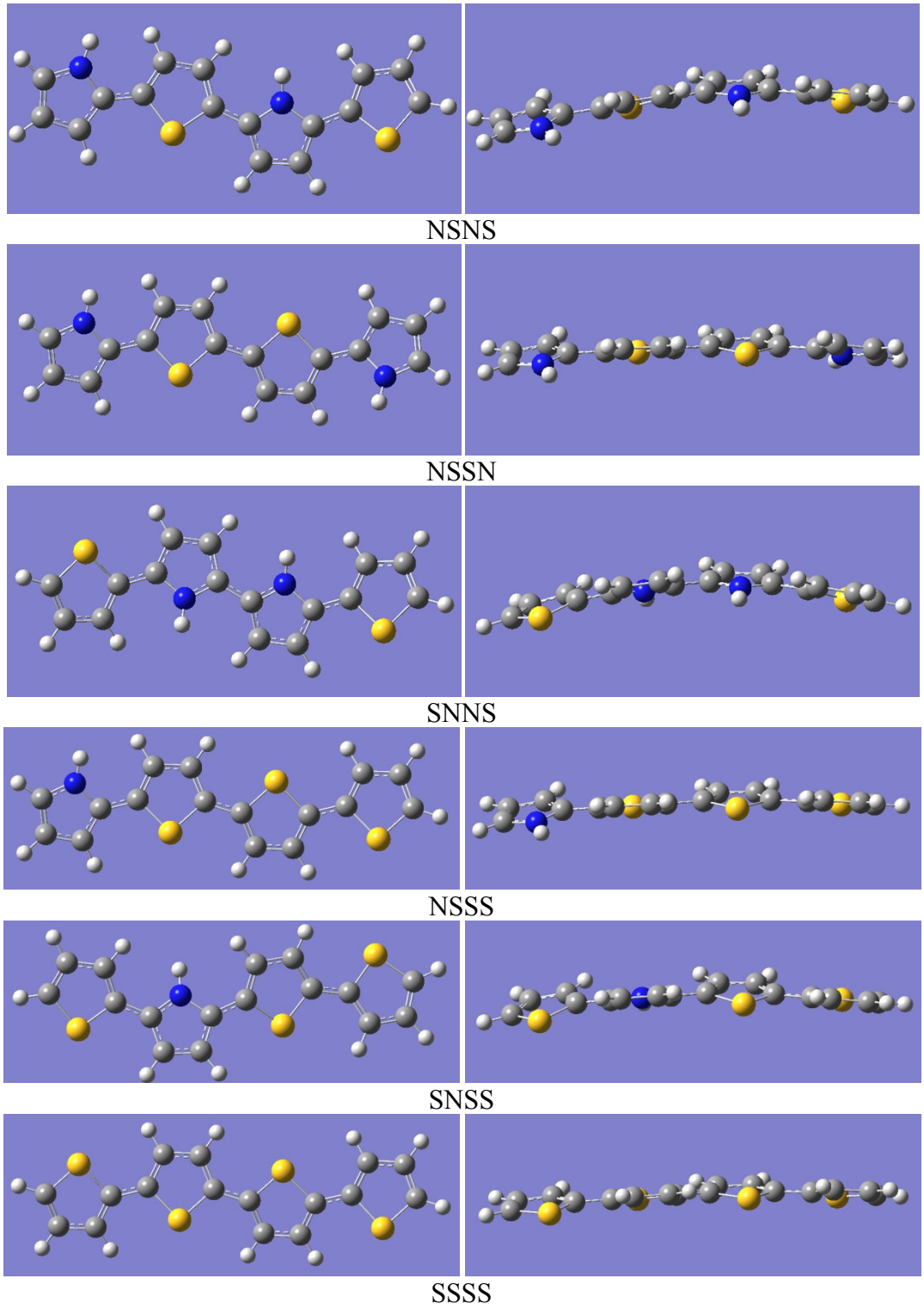


**Fig. S2** Optimized structures of the oligomers; N and S denote pyrrole ring and thiophene ring in the oligomers, respectively.

Fig. S2 shows the optimized structures of the oligomers containing N and S with monomer number more than 2. It is found that the trimers have planar configurations while the tetramers have configurations in a relatively curved form. Also, the bending of the oligomer configurations increases as the number of N increases. This can be reflected by the configurations of SSSS, SNSS, NSSS, SNNS, NSSN, NSNS, NNSS, NNSN, and NNNS, especially for the configurations with N lying in the middle of oligomer chain such as SNNS and NNNS. This result indicates that the introduction of N into copolymer is beneficial for enhancing the flexibility of polymer chain.

## S4. XPS data

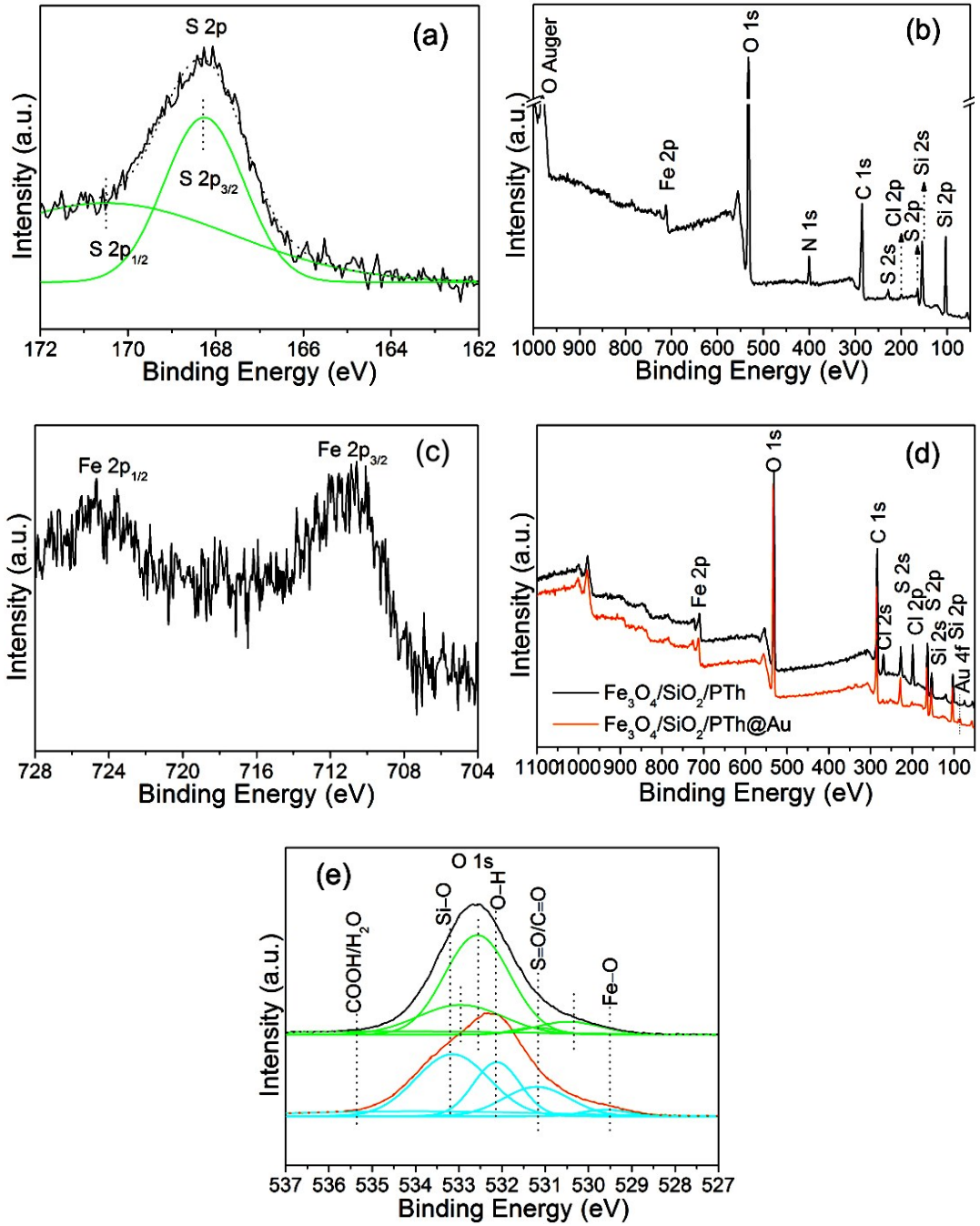


**Fig. S3** (a) S 2p spectrum of the sample prepared with $(NH_4)_2S_2O_8$, pyrrole, and thiophene in aqueous medium; (b) survey spectrum of $Fe_3O_4/SiO_2$/cPPyTh; (c) Fe 2p of $Fe_3O_4/SiO_2$/cPPyTh; (d) survey spectrum of $Fe_3O_4/SiO_2$/PTh and $Fe_3O_4/SiO_2$/PTh@Au; (e) O 1s of $Fe_3O_4/SiO_2$/cPPyTh before (black and green lines) and after Au(III) adsorption (red and cyan lines).

**Table S2** Results of XPS analysis.

| sample | C 1s | | | | N 1s | | | | Au 4f | |
|---|---|---|---|---|---|---|---|---|---|---|
| | Component (eV)/concentration (%) | | | | Component (eV)/concentration (%) | | | | Component (eV)/concentration | |
| $Fe_3O_4/SiO_2$/cPPyTh | 284.5/32.6 | 285.5/29.5 | 287.8/29.2 | 291.3/8.7 | 399.4/22.0 | 400.0/41.1 | 400.6/17.1 | 401.9/19.8 | – | – |
| $Fe_3O_4/SiO_2$/cPPyTh@Au | 284.8/23.4 | 286.1/7.2 | 287.9/9.8 | 290.4/59.6 | 399.6/18.3 | 400.0/14.8 | 400.5/29.1 | 405.1/37.8 | 84.2/53.2 | 87.8/46.8 |
| $Fe_3O_4/SiO_2$/PPy | 284.7/57.0 | 287.1/27.4 | 291.1/15.6 | | 399.2/9.6 | 399.7/26.3 | 400.1/43.7 | 402.2/20.4 | – | – |
| $Fe_3O_4/SiO_2$/PPy@Au | 284.7/55.3 | 287.2/33.3 | 291.4/11.4 | | 399.4/28.6 | 399.9/44.1 | 400.4/19.1 | 402.5/8.2 | 83.7/54.1 | 87.4/45.9 |
| $Fe_3O_4/SiO_2$/PTh | 284.7/68.2 | 285.9/13.9 | 288.2/17.9 | | – | – | – | – | – | – |
| $Fe_3O_4/SiO_2$/PTh@Au | 284.8/71.7 | 286.1/12.8 | 288.3/15.5 | | – | – | – | – | 84.1/54.5 | 87.8/45.5 |
| assignment | C=C/C=N | C–S(Cl) | C–O | C=O | C=N | N–H | $C–N^+$ | $C=N^+$ | Au $4f_{7/2}$ | Au $4f_{5/2}$ |

| sample | S 2p | | | O 1s | | | | |
|---|---|---|---|---|---|---|---|---|
| | Component (eV)/concentration (%) | | | Component (eV)/concentration (%) | | | | |
| $Fe_3O_4/SiO_2$/cPPyTh | 163.8/33.4 | 165.0/31.3 | 168.3/35.3 | 530.4/7.2 | 531.2/2.7 | 532.6/50.4 | 532.8/32.0 | 534.4/7.7 |
| $Fe_3O_4/SiO_2$/cPPyTh@Au | 163.9/37.7 | 165.2/14.3 | 168.8/48.0 | 529.6/2.8 | 531.2/18.4 | 532.1/23.8 | 533.1/42.9 | 534.0/12.1 |
| $Fe_3O_4/SiO_2$/PTh | 163.8/34.5 | 164.8/65.5 | – | | | | | |
| $Fe_3O_4/SiO_2$/PTh@Au | 163.9/33.0 | 164.9/67.0 | – | | | | | |
| assignment | S $2p_{3/2}$ | S $2p_{1/2}$ | oxysulfide | Fe–O | C=O/S=O | O–H | Si–O | $COOH/H_2O$ |

## S5. CHNS analysis

**Table S3** Results of CHNS analysis.

| sample | weight (mg) | weight percent of every element (wt%) | | | | atomic ratio of N/S |
|---|---|---|---|---|---|---|
| | | N | C | S | H | |
| $Fe_3O_4/SiO_2$/cPPyTh (5:1) | 2.2030 | 9.344 | 35.43 | 1.517 | 6.044 | 14.1 |
| $Fe_3O_4/SiO_2$/cPPyTh (3:1) | 2.6180 | 8.852 | 34.28 | 1.677 | 5.399 | 12.1 |
| $Fe_3O_4/SiO_2$/cPPyTh (1:1) | 2.6480 | 4.232 | 22.81 | 5.111 | 3.306 | 1.9 |
| $Fe_3O_4/SiO_2$/cPPyTh (1:5) | 3.5840 | 3.028 | 23.72 | 8.740 | 3.413 | 0.8 |

## S6. FT-IR analysis

**Table S4** Results of FT-IR analysis.

| sample | peak position ($cm^{-1}$) | | | | | | | |
|---|---|---|---|---|---|---|---|---|
| $Fe_3O_4/SiO_2$/PPy | | 1555, 1464 | 1190 | 926, 792, 668 | 1097, 478, 967 | 1317 | | 575 |
| assignment | | ring breathing | C–OH | C–H | Si–O–Si/H | C–N | | Fe–O |
| $Fe_3O_4/SiO_2$/PTh | 1701 | (1555, 1464)/1514 | 1190 | 926, 798 | 1097, 468, 967 | 709 | 618 | 576 |
| assignment | C=O | ring/p-doped ring breathing | C–OH | C–H | Si–O–Si/H | C–Cl | C–S | Fe–O |
| $Fe_3O_4/SiO_2$/cPPyTh | 1701 | 1564, 1479 | 1206, 1119 | 932, 796, 668 | 1097, 478, 967 | | 618 | 575 |
| assignment | C=O | ring breathing | C–OH | C–H | Si–O–Si/H | | C–S | Fe–O |
| ref. | | 1,5,6 | | 1,5 | 3-5 | 7 | 5 | 3 |

## S7. Cyclic voltammograms (CVs)

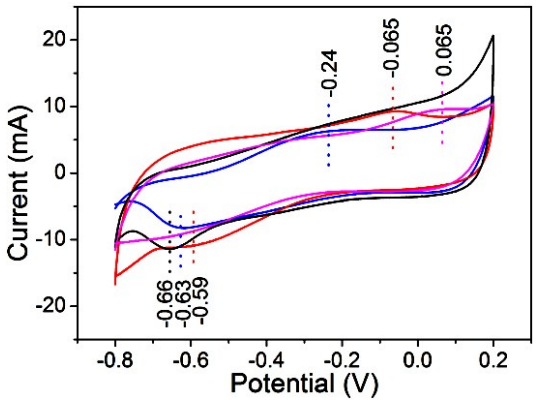


**Fig. S4** CVs of cPPyTh (black line), PPy (blue line), and PTh (red line) at a scan rate of 10 mV $s^{-1}$; the magenta line corresponds to the CV of the blending of PPy with PTh.

Fig. S4 shows the CVs of the samples. It is apparent that the CV of cPPyT is different from that of PPy, PTh, and the blending of PPy with PTh. The cathodic peaks are centered at –0.66, –0.63, and –0.59 V for cPPyTh, PPy, and PTh, respectively, whereas there is no apparent cathodic peaks in the CV of the blending of PPy with PTh. This result reflects the formation of copolymer of pyrrole–thiophene.

## S8. Determination of weight percentage of the nonmagnetic components

Through the TG analysis (Fig. S5), the weight percentage of the polymer in the nanocomposites is estimated to be 51.4%, 49.2%, and 47.7% for $Fe_3O_4/SiO_2$/cPPyTh, $Fe_3O_4/SiO_2$/PPy, and $Fe_3O_4/SiO_2$/PTh, respectively. Also, the weight percentage of $SiO_2$ in $Fe_3O_4/SiO_2$ is determined to be 33.8% through the ICP–OES technique, using hydrofluoric acid to dissolve $Fe_3O_4/SiO_2$ powders. Therefore, the weight percentage of the nonmagnetic components is ca. 67.8%, 65.6%, and 64.1% for $Fe_3O_4/SiO_2$/cPPyTh, $Fe_3O_4/SiO_2$/PPy, and $Fe_3O_4/SiO_2$/PTh, respectively.

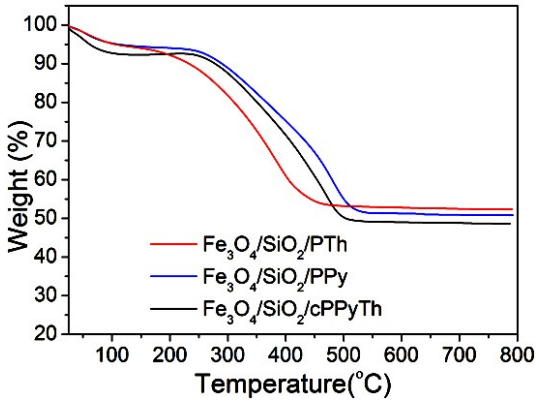


**Fig. S5** TG curves of the samples.

**S9. Magnetic response of $Fe_3O_4/SiO_2$/cPPyTh from Au(III) solution through a hand-held magnet**

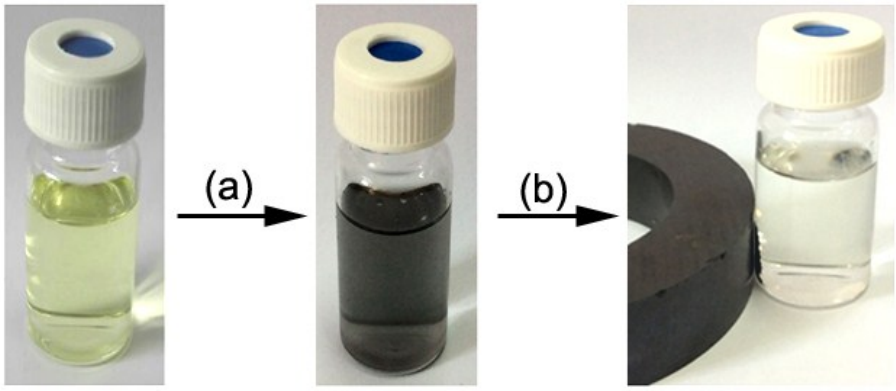


**Fig. S6** (a) photo taken for addition of $Fe_3O_4/SiO_2$/cPPyTh (2 mg) into Au(III) aqueous solution (90 mg $L^{-1}$, 10 mL) after vibration for 1 min, presenting a good dispersion; (b) photo taken after magnetic separation for 3 min with a hand-held magnet, offering a nearly colorless liquid.

## S10. BET analysis

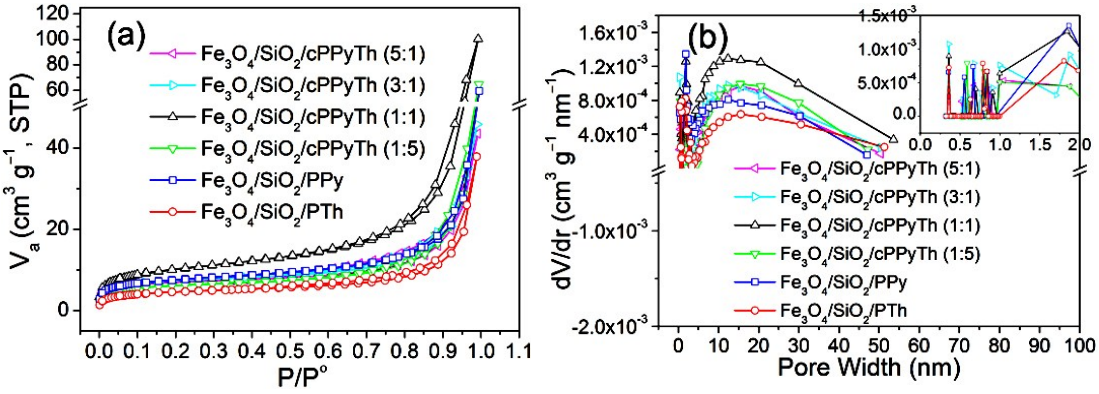


**Fig. S7** (a) Sorption isotherms; (b) pore size distribution plots of the adsorbents.

**Table S5** BET analysis results of the samples.

| sample | $S_{BET}$ ($m^2\ g^{-1}$) | total volume in pores ($cm^3\ g^{-1}$) | *t*-plot micropore area ($m^2\ g^{-1}$) | $S_{micro}/S_{BET}$ |
|---|---|---|---|---|
| $Fe_3O_4/SiO_2$/cPPyTh (5:1) | 24.6 | 0.053 | 13.3 | 54.1% |
| $Fe_3O_4/SiO_2$/cPPyTh (3:1) | 25.9 | 0.055 | 12.5 | 48.3% |
| $Fe_3O_4/SiO_2$/cPPyTh (1:1) | 36.0 | 0.033 | 9.8 | 27.2% |
| $Fe_3O_4/SiO_2$/cPPyTh (1:5) | 22.0 | 0.072 | 7.9 | 35.9% |
| $Fe_3O_4/SiO_2$/PPy | 26.9 | 0.066 | 10.1 | 37.5% |
| $Fe_3O_4/SiO_2$/PTh | 16.4 | 0.043 | 5.5 | 33.5% |

## S11. Adsorption properties of the samples

*S11.1 Effect of solution pH*

The distribution of negatively charged Au(III) species, such as $AuCl_4^-$, $AuCl_3(OH)^-$, $AuCl_2(OH)_2^-$, $AuCl(OH)_3^-$, and $Au(OH)_4^-$, is highly pH-dependent.[8] As the solution pH increases, the concentration of more hydroxyated Au(III) species increases concomitant with the decrease in concentration of both $AuCl_4^-$ and less hydroxyated Au(III) species, according to the following sequences:

$$AuCl_4^- \xrightarrow{OH^-} AuCl_3(OH)^- \xrightarrow{OH^-} AuCl_2(OH)_2^- \xrightarrow{OH^-} AuCl(OH)_3^- \xrightarrow{OH^-} Au(OH)_4^-$$

To evaluate the effect of solution pH on Au(III) recovery, 1 mg of sample powders were dispersed into an aliquot of 10 mL of Au(III) solution (90 mg $L^{-1}$) with pH ranging from 2 to 5.5. The solution pH was adjusted through addition of anhydrous sodium acetate. The dispersions were oscillated in a constant-temperature water-bathing vibrator (HZ-9613Y, Jiangsu, China) for 12 h, operating with a reciprocating vibration rate of 100 rpm at room temperature. After magnetic separation, the supernates were sampled and analyzed on a PerkinElmer Optima 7000DV inductively coupled plasma–optical emission spectrometer (ICP–OES).

For $Fe_3O_4/SiO_2$/PTh, the equilibrium adsorption capacity ($Q_e$) of the adsorbent monotonously increases with increasing pH from 2 to 5.5 (Fig.S8a). In the case of $Fe_3O_4/SiO_2$/cPPyTh and $Fe_3O_4/SiO_2$/PPy, the $Q_e$ gradually increases with increasing pH from 2 to 4 and then stabilizes at the pH range of 4–5.5.

According to the ζ-potential plots (Fig. 4B in the text), the positive charges upon the adsorbents decrease as the solution pH increases, rendering isoelectric points at 3.4, 3.8, and 6.1 for $Fe_3O_4/SiO_2$/PTh, $Fe_3O_4/SiO_2$/cPPyTh, and $Fe_3O_4/SiO_2$/PPy, respectively. This result indicates that the increase in solution pH does not favour adsorption of Au(III) upon the adsorbents, due to electrostatic repulsion. However, the equilibrium adsorption capacity ($Q_e$) of the adsorbents increases with increasing pH from 2 to 5.5 (Fig.S8a). Further increase in solution pH over 5.5 may cause

solution turbid, probably due to the formation of insoluble gold acetate. As a result, we performed Au(III) recovery from solution with pH 5 in the continued experiments.

As documented in literature,[8] the existing forms of Au(III) species in solution with pH 5 are mainly $AuCl_4^-$ and $AuCl_3(OH)^-$, accompanying with a small amount of $AuCl_2(OH)_2^-$. Also, complexation between Au(III) and N/S heteroatoms is weakly sensitive to solution pH.[2] Therefore, the adsorption of Au(III) species upon the N-containing adsorbents is mainly controlled by hydrogen bonding and complexation between Au(III) and heterocycles, rather than by electrostatic interactions. As for Au(III) adsorption upon $Fe_3O_4/SiO_2$/PTh, both complexation and ion exchange between $Cl^-$ and gold anions are responsible for the adsorption process. This is reflected by the XPS result (Fig. S3d), where signals of elemental chlorine are almost eliminated after Au(III) recovery.

*S11.2 Adsorption kinetics*

Fig.S8b shows the kinetics plots of $Q_t$ versus $t$, where $Q_t$ represents the adsorption capacity (mg $g^{-1}$) at time of $t$ (min). It is found that the time for the adsorbents to reach adsorption equilibrium is ca. 4 h. All the $Fe_3O_4/SiO_2$/cPPyTh samples with different N/S ratios exhibit superior equilibrium adsorption capacity ($Q_e$) compared with $Fe_3O_4/SiO_2$/PPy and $Fe_3O_4/SiO_2$/PTh. Also, the $Q_e$ values gradually increase from 803.5 to 845.9 mg $g^{-1}$ as the N/S ratio increases from 0.8 to 12 (Fig. S8b inset). Further increase in N/S ratio does not favour the increase in $Q_e$ value. The $Fe_3O_4/SiO_2$/cPPyTh sample with N/S of 12 corresponds to the sample synthesized with pyrrole/thiophene (Py/Th) molar ratio of 3 in the starting materials, and named $Fe_3O_4/SiO_2$/cPPyTh (3:1). More significantly, the adsorption capacity dramatically increases to 559.7, 516.1, 496.7, 310.2, 259.4, and 193.7 mg $g^{-1}$ within 5 min, and reaches 66.2%, 61.8%, 60.8%, 38.6%, 57.4%, and 47.6% of the $Q_e$ for $Fe_3O_4/SiO_2$/cPPyTh (3:1), $Fe_3O_4/SiO_2$/cPPyTh (5:1), $Fe_3O_4/SiO_2$/cPPyTh (1:1), $Fe_3O_4/SiO_2$/cPPyTh (1:5), $Fe_3O_4/SiO_2$/PPy, and $Fe_3O_4/SiO_2$/PTh in sequence. The rapid enrichment of Au(III) species upon the magnetic adsorbents is beneficial for Au(III) recovery with high throughput. To reveal further information on adsorption of Au(III) upon the adsorbents, the adsorption kinetics data are

analyzed with Lagergren pseudo-first order,[9] pseudo-second order,[9] Elovich,[10] and intraparticle diffusion kinetics models,[11] whose linear forms are presented from eq 6 to eq 9, respectively.

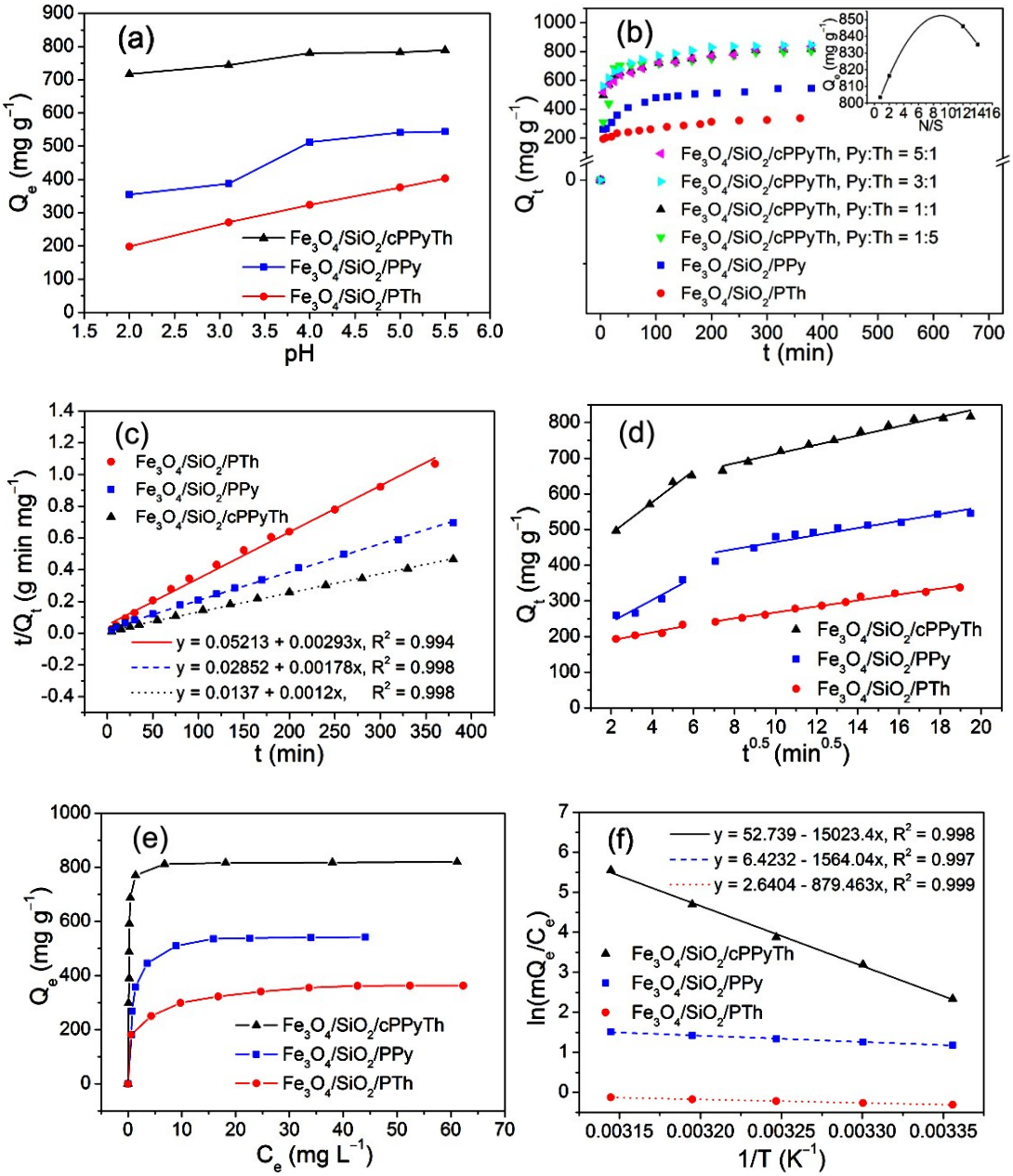


**Fig. S8** (a) Equilibrium adsorption capacity of the adsorbents as a function of solution pH; (b) kinetics plots; inset in b is the plot of $Q_e$ versus N/S atomic ratio; (c) plots derived from the pseudo-second order kinetics model; (d) plots derived from the intraparticle diffusion model; (e) adsorption isotherms; (f) plots of ln($mQ_e/C_e$) versus 1/$T$.

$$\ln (Q_e - Q_t) = lnQ_e - k_1 t \quad (6)$$

$$\frac{t}{Q_t} = \frac{1}{k_2 Q_e^2} + \frac{t}{Q_e} \quad (7)$$

$$Q_t = \frac{1}{\beta}\ln(\alpha\beta) + \frac{1}{\beta}ln(t) \quad (8)$$

$$Q_t = k_{id}t^{0.5} + C \quad (9)$$

where $k_1$, $k_2$, and $k_{id}$ represent the corresponding rate constant; $\alpha$ is the initial adsorption rate; $\beta$ and $C$ are constants related to desorption and the thickness of boundary layer, respectively.

In general, the adsorption capacity of an adsorbent is related to the surface functionalities and textural parameters such as specific surface area ($S_{BET}$) and pore size distribution (PSD). After examination by the BET method, the $S_{BET}$ of the adsorbents is determined to be 24.6, 25.9, 36.0, 22.0, 26.9, and 16.4 $m^2\ g^{-1}$ for $Fe_3O_4/SiO_2$/cPPyTh (5:1), $Fe_3O_4/SiO_2$/cPPyTh (3:1), $Fe_3O_4/SiO_2$/cPPyTh (1:1),$Fe_3O_4/SiO_2$/cPPyTh (1:5), $Fe_3O_4/SiO_2$/PPy, and $Fe_3O_4/SiO_2$/PTh in sequence (Table S5). In association with the adsorption behaviors of the adsorbents toward Au(III) species (Fig. S8b), there is no simple relationship between the adsorption capacity and the $S_{BET}$. Nevertheless, the $Fe_3O_4/SiO_2$/cPPyTh (5:1, 3:1, and 1:5) samples with $S_{BET}$ close to that of $Fe_3O_4/SiO_2$/PPy have superior $Q_e$ values to that of the latter. This result reveals that the coexistence of N and S makes a positive contribution to the adsorption capacity of the adsorbents. As determined by the CV measurements (Fig. S4), the upper band of the lowest unoccupied molecular orbital (LUMO) level for cPPyTh is higher than that for PPy and PTh (*page 5 in the text*), a situation that is beneficial for Au(III) recovery upon $Fe_3O_4/SiO_2$/cPPyTh through an adsorption–reduction mechanism. For $Fe_3O_4/SiO_2$/cPPyTh samples, the equilibrium adsorption capacity increases as the N/S ratio increases from 0.8 to 12, and then decreases with increasing N/S ratio to 14. This result indicates that there exists an optimal N/S ratio for $Fe_3O_4/SiO_2$/cPPyTh serving as adsorbents for Au(III) recovery (Fig. S8b inset). The existence of an optimal N/S ratio is attributed to the synergistic effect offered by the lower oxidation potential of pyrrole ring compared with thiophene ring but the higher affinity of S to gold ion species compared with N. For the adsorbents containing individual N or S heteroatoms, the superior adsorption capacity of $Fe_3O_4/SiO_2$/PPy is attributed to the relatively larger $S_{BET}$, lower

oxidation potential of pyrrole ring compared with thiophene ring, and to the linkage of amino groups with hydroxylated gold species (such as $AuCl_3(OH)^-$ and $AuCl_2(OH)_2^-$) through hydrogen bonding. Also, it is found that the *t*-plot micropore area ($S_{micro}$) positively contributes to the adsorption capacity. This is reflected by Table S5, where the $S_{micro}/S_{BET}$ for $Fe_3O_4/SiO_2$/cPPyTh (5:1, 3:1, and 1:5) is higher than that for $Fe_3O_4/SiO_2$/PPy and that for $Fe_3O_4/SiO_2$/PTh in sequence. As shown in Fig. S7b, the samples exhibit a multimodal characteristic. The existence of micropores can be reflected by the abrupt sorption plateau at the $P/P°$ range of 0.1–0.6 (Fig. S7a).[12] The hysteresis at $P/P°$ over 0.8 is due to the macropores arising from particle aggregation. The micropores determined by the non-local density function theory (NLDFT) model are concentrated at 0.55–0.91 nm, and the mesopores determined by the Barrett–Joyner–Halenda (BJH) model are concentrated around ca. 15 nm, respectively (Fig. S7b and inset). The porous characteristic is beneficial for Au(III) adsorption through intraparticle diffusion (discussion below).

In view of the similar adsorption behaviors of the $Fe_3O_4/SiO_2$/cPPyTh samples with close $Q_e$ value (Fig. S8b), we select $Fe_3O_4/SiO_2$/cPPyTh with Py/Th ratio of 1:1 as an example for further investigation. According to the results derived from the kinetics models (Table S6), the values of $R^2$ for the pseudo-second order approach to 1 and are higher than those for the other models (Fig.S8c). Moreover, the calculated values of equilibrium adsorption capacity ($Q_{e,cal}$) approach nearer to the experimental values ($Q_{e,exp}$) according to the pseudo-second order kinetics model. Therefore, we conclude the adsorption of Au(III) upon the adsorbents preferably follows the pseudo-second order kinetics model. It is also found that the adsorbent with relatively higher $Q_{e,exp}$ has a relatively smaller $k_2$ but a relatively higher initial adsorption rate ($r_i$), which can be calculated by eq 10.[13]

$$r_i = k_2 Q_e^2 \quad (10)$$

**Table S6** Kinetics parameters for Au(III) adsorption upon the adsorbents.

| kinetics model | parameter | adsorbent | | |
|---|---|---|---|---|
| | | $Fe_3O_4/SiO_2$/cPPyTh | $Fe_3O_4/SiO_2$/PPy | $Fe_3O_4/SiO_2$/PTh |
| pseudo-first order | $k_1$ ($min^{-1}$) | $1.224\times10^{-2}$ | $1.213\times10^{-2}$ | $8.32\times10^{-3}$ |
| | $Q_{e,cal}$ (mg $g^{-1}$) | 323.0 | 287.2 | 150.8 |
| | $R^2$ | 0.947 | 0.922 | 0.983 |
| pseudo-second order | $k_2$ (g $mg^{-1}$ $min^{-1}$) | $1.05\times10^{-4}$ | $1.11\times10^{-4}$ | $1.65\times10^{-4}$ |
| | $r_i$ (mg $g^{-1}$ $min^{-1}$) | 72.9 | 35.1 | 19.2 |
| | $Q_{e,exp}$ (mg $g^{-1}$) | 816.3 | 545.5 | 337.4 |
| | $Q_{e,cal}$ (mg $g^{-1}$) | 833.3 | 561.8 | 341.3 |
| | $R^2$ | 0.998 | 0.998 | 0.994 |
| Elovich | $\alpha$ (mg $g^{-1}$ $min^{-2}$) | $1.13\times10^{4}$ | 338.8 | 967.1 |
| | $\beta$ (mg $g^{-1}$ $min^{-1}$) | $1.34\times10^{-2}$ | $1.33\times10^{-2}$ | $2.85\times10^{-2}$ |
| | $R^2$ | 0.992 | 0.974 | 0.937 |
| intraparticle diffusion | $k_{id}$ (mg $g^{-1}$ $min^{-1}$) | 16.8 | 17.3 | 8.85 |
| | $R^2$ | 0.916 | 0.875 | 0.987 |

Based on the results from the Elovich model, the relatively high $\alpha$ values indicate covalent combination between Au(III) species and the adsorbents through coordination bonding,[11] especially for the S-containing adsorbents. In addition, the plots derived from the intraparticle diffusion model exhibit a multilinear feature (Fig.S8d). This indicates the adsorption process involves two or more steps.[9] The first linear portions with relatively high slope represent the rapid adsorption through macropore diffusion, and the second linear portions correspond to adsorption through mesopore/micropore diffusion. The multimodal porous characteristic of the adsorbents can be reflected by their PSD plots (Fig. S7b).

*S11.3 Adsorption isotherms*

Fig. S8e shows the adsorption isotherms of the adsorbents toward Au(III). The Langmuir,[1,4] Freundlich,[1,4] and Dubinin–Radushkevich (D–R)[1,14] isotherm equations are used to interpret the

adsorption data. The Langmuir model assumes that the uptake of metal ions occurs on a homogeneous surface by monolayer adsorption without any interaction between adsorbed ions.[4] The Langmuir isotherm equation is expressed as eq 1:

$$\frac{C_e}{Q_e} = \frac{1}{K_L Q_m} + \frac{C_e}{Q_m} \quad (1)$$

where $C_e$ is the equilibrium concentration of Au(III) in the supernate (mg $L^{-1}$); $Q_e$ is the equilibrium adsorption capacity of the adsorbents (mg $g^{-1}$); $Q_m$ represents the maximum adsorption capacity of the adsorbents (mg $g^{-1}$), and $K_L$ the Langmuir constant (L $mg^{-1}$).

**Table S7** Adsorption isotherm parameters for Au(III) uptake upon the adsorbents.

| isotherm model | parameter | adsorbent | | |
|---|---|---|---|---|
| | | $Fe_3O_4/SiO_2$/cPPyTh | $Fe_3O_4/SiO_2$/PPy | $Fe_3O_4/SiO_2$/PTh |
| Langmuir | $Q_m$ (mg $g^{-1}$) | 819.7 | 555.6 | 374.5 |
| | $K_L$ (L $mg^{-1}$) | 7.51 | 1.18 | 0.52 |
| | $R^2$ | 0.999 | 0.999 | 0.999 |
| Freundlich | $K_F$ (mg $g^{-1}$) | 574.8 | 280.6 | 202.8 |
| | $n$ | 8.65 | 4.72 | 6.49 |
| | $R^2$ | 0.567 | 0.779 | 0.979 |
| Dubinin–Radushkevich | $Q_m$ (mg $g^{-1}$) | 939.2 | 647.8 | 377.1 |
| | $\beta$ ($mol^2$ $J^{-2}$) | $2.45\times10^{-3}$ | $4.9\times10^{-3}$ | $3.6\times10^{-3}$ |
| | $E$ (kJ $mol^{-1}$) | 14.3 | 10.1 | 11.8 |
| | $R^2$ | 0.729 | 0.873 | 0.974 |

The Freundlich model assumes that sorption occurs on a heterogeneous surface by monolayer adsorption.[4,14] The Freundlich isotherm equation is expressed as eq 2:

$$\ln Q_e = \ln K_F + \frac{1}{n} \ln C_e \quad (2)$$

where $K_F$ is the Freundlich constant reflecting the adsorption capacity of the adsorbents (mg $g^{-1}$), and $n$ is an empirical parameter related to the intensity of adsorption. For a favorable adsorption process,

the value of $n$ should lie in the range of 1–10.[14]

The D–R model is also based on sorption occurring on a heterogeneous surface. Using the D–R model, we can differentiate between physical and chemical adsorption.[14] The D–R isotherm equation is expressed as eq 3:

$$\ln Q_e = \ln Q_m - \beta\varepsilon^2 \quad (3)$$

where $\beta$ is the activity coefficient related to mean adsorption energy (mol$^2$ J$^{-2}$), and $\varepsilon$ is the Polanyi potential (kJ$^2$ mol$^{-2}$), which is represented as eq 4:

$$\varepsilon = RT\ln\left(1 + \frac{1}{C_e}\right) \quad (4)$$

where $R$ is the gas constant (8.314 J mol$^{-1}$ K$^{-1}$) and $T$ the absolute temperature (K). The mean adsorption energy $E$ (kJ mol$^{-1}$) can be calculated by eq 5:

$$E = \frac{1}{\sqrt{2\beta}} \quad (5)$$

The value of $E$ gives useful information on the type of adsorption. When the value of $E$ lies in the range of 8–16 kJ mol$^{-1}$, chemical adsorption occurs. If the value is smaller than 8 kJ mol$^{-1}$, the adsorption proceeds physically.[14]

The adsorption isotherm parameters for Au(III) uptake upon the adsorbents are provided in Table S7. Through comparison in the linear fitting correlation coefficients ($R^2$) of the isotherm models, we conclude that the adsorption of Au(III) species upon the adsorbents conforms to the Langmuir isotherm model rather than the Freundlich or D–R model. Also, the $Q_m$ values of the adsorbents derived from the Langmuir model agree well with their experimental $Q_e$ values (Fig.S8b), consolidating the above conclusion.

The $Q_m$ values of the adsorbents are much higher than that of magnetic adsorbents in previous reports,[2,15-17] where $Q_m$ values are usually smaller than 200 mg g$^{-1}$. Moreover, $Fe_3O_4/SiO_2$/cPPyTh exhibits superior adsorption capacity to that of many other nonmagnetic adsorbents,[18-22] as listed in

Table S8. Considering that cPPyTh shell accounts for 51.4 wt.% of the adsorbent, the $Q_m$ value of cPPyTh is estimated to be 1594.7 mg $g^{-1}$, comparable to that of 1491.3 mg $g^{-1}$ for cross-linked cellulose gels.[23] In addition, from the viewpoint of the Freundlich and D–R models, chemisorption dominates the favorable adsorption of Au(III) species upon the adsorbents. This is because the values of *n* and *E* lie in the range of 1–10 and 8–16 kJ $mol^{-1}$ (Table S6), respectively.[14]

**Table S8** Comparison in adsorption capacity of the adsorbents.

| adsorbent | $Q_m$ (mg $g^{-1}$) | ref. |
|---|---|---|
| $Fe_3O_4/SiO_2$/cPPyTh | 819.7 | this work |
| $Fe_3O_4/SiO_2$/PPy | 555.6 | this work |
| $Fe_3O_4/SiO_2$/PTh | 374.5 | this work |
| C/Co nanoparticles | 72 | 15 |
| MPTS-modified cobalt ferrite nanoparticles | 120.5 | 16 |
| $Fe_3O_4$/fir sawdust composite | 188.7 | 17 |
| SH-modified $Fe_3O_4/SiO_2$ nanoparticles | 84.8 | 2 |
| Hydrothermal carbon spherules | 504.3 | 28 |
| Melamine–formaldehyde–thiourea chelating resin | 48 | 31 |
| Glutaraldehyde-crosslinked chitosan beads | 280 | 29 |
| polystyrene-supported bis-8-oxyquinoline-terminated open-chain crown ether | 614.6 | 18 |
| 2-aminothiazole functionalized polystyrene | 713.8 | 19 |
| Graphene oxide | 108.3 | 13 |
| Thiol-ene photoclick hydrogels | 125 | 20 |
| Aminomethyl pyridine-modified cellulose | 537.8 | 21 |
| Cross-linked cellulose gels | 1491.3 | 22 |

*S11.4 Adsorption thermodynamics*

To determine whether the adsorption of Au(III) upon the adsorbents proceeds spontaneously, the adsorption experiments were also performed at 30, 35, 40, and 45 °C for 4 h. The adsorption thermodynamics data are analyzed with eqs 11 and 12:[23]

$$\ln \frac{mQ_e}{C_e} = \frac{\Delta S°}{R} - \frac{\Delta H°}{RT} \quad (11)$$

$$\Delta G° = -RT ln\left(\frac{mQ_e}{C_e}\right) \quad (12)$$

where $\Delta S°$ (J mol$^{-1}$ K$^{-1}$), $\Delta H°$ (kJ mol$^{-1}$), and $\Delta G°$ (kJ mol$^{-1}$) are the variations in standard entropy, enthalpy, and in Gibbs energy, respectively; $m$ is the dose of the adsorbent (g L$^{-1}$), and the ratio of $mQ_e/C_e$ is referred to as adsorption affinity.

**Table S9** Thermodynamics parameters for Au(III) adsorption upon the adsorbents.

| adsorbent | $\Delta S°$ (J mol$^{-1}$ K$^{-1}$) | $\Delta H°$ (kJ mol$^{-1}$) | $\Delta G°$ (kJ mol$^{-1}$)/$Q_e$ (mg g$^{-1}$) at different temperatures (K) | | | | |
|---|---|---|---|---|---|---|---|
| | | | 298 | 303 | 308 | 313 | 318 |
| $Fe_3O_4/SiO_2$/cPPyTh | 438.5 | 15.02 | –5.79/816.3 | –8.05/859.5 | –9.98/865.0 | –12.23/869.7 | –14.68/874.8 |
| $Fe_3O_4/SiO_2$/PPy | 53.4 | 1.56 | –2.93/545.5 | –3.17/597.2 | –3.43/606.4 | –3.70/618.3 | –4.00/634.2 |
| $Fe_3O_4/SiO_2$/PTh | 22.0 | 0.88 | 0.77/337.4 | 0.66/346.9 | 0.55/353.7 | 0.44/356.1 | 0.33/366.3 |

Fig.S8f shows the plots of ln($mQ_e/C_e$) versus 1/$T$. The values of $\Delta G°$, $\Delta S°$, and $\Delta H°$ in Table S9 are determined with eq 12 and by linear fitting the plots in Fig.S8f. It is found that the adsorbent having relatively higher $Q_e$ values possesses relatively higher $\Delta S°$ and $\Delta H°$ values for Au(III) adsorption. The positive values of $\Delta S°$ and $\Delta H°$ reflect endothermic adsorption with increase in degree of disorder at the adsorbent/liquid interface.[23] The negative $\Delta G°$ values along with decrease in $\Delta G°$ with increasing temperature indicate spontaneous adsorption of Au(III) upon the adsorbents. However, the adsorption of Au(III) upon $Fe_3O_4/SiO_2$/PTh presents positive $\Delta G°$ values, suggesting non-spontaneous adsorption processes at the measured temperature range (25–45 °C). Reminding of the surface of $Fe_3O_4/SiO_2$/PTh in solution with pH 5 is more negatively charged in comparison with that of N-containing adsorbents, the non-spontaneous adsorption is attributed to the relatively strong electrostatic repulsion between $Fe_3O_4/SiO_2$/PTh and Au(III) species.

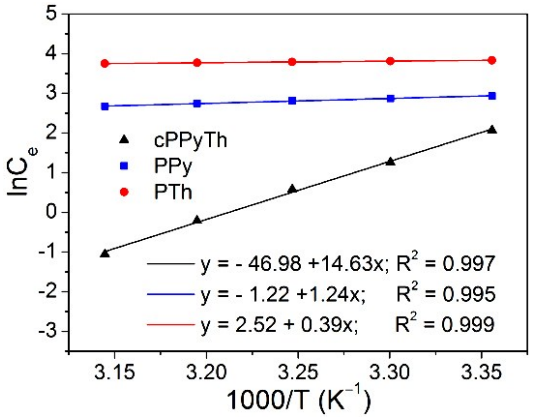


**Fig. S9** Plots of ln$C_e$ versue 1/$T$.

*S11.5 Apparent isosteric heat of adsorption*

Apparent isosteric heat of adsorption ($\Delta H_a$) is well accepted as an indicator of the type of adsorption force. The values of $\Delta H_a$ can be calculated with the Clausius–Clapeyron equation:[24-26]

$$\frac{\mathrm{d}\ln C_e}{\mathrm{d}T} = \frac{\Delta H_a}{RT^2} \quad (13)$$

$$\ln C_e = -\frac{\Delta H_a}{RT} + C \quad (14)$$

where $C_e$ is the equilibrium concentration of Au(III) in the supernate (mg $L^{-1}$) at different temperatures; $R$ is the gas constant (8.314 J $mol^{-1}$ $K^{-1}$); $T$ is the solution temperature in Kelvin (K), and $C$ the integration constant.

Fig. S9 shows the plots of ln$C_e$ versus 1/$T$ according to eq 14. The fitting curves of the plots offer high correlation coefficients, giving $-\Delta H_a$ values of 121.6, 10.3, and 3.24 kJ $mol^{-1}$ for Au(III) adsorption upon $Fe_3O_4/SiO_2$/cPPyTh, $Fe_3O_4/SiO_2$/PPy, and $Fe_3O_4/SiO_2$/PTh, respectively. Usually, the $-\Delta H_a$ for physisorptions is smaller than 16.7 kJ $mol^{-1}$, and that for chemisorptions is higher than 37.7 kJ $mol^{-1}$.[24] However, the $-\Delta H_a$ for adsorbate upon adsorbent is highly dependent on the concentration of adsorbate in solution,[25,26] making it difficult to determine the type of adsorption by virtue of apparent isosteric heat of adsorption at a specific adsorbate concentration in solution. As mentioned before, the type of adsorption can be evaluated from the viewpoint of the Freundlich and D–R models.

## S12. Calculation results of $S_{Au}$ versus interfering ions

**Table S10** Calculation results of $S_{Au}$ versus interfering ions with different adsorbent doses.

| adsorbent | ion | $S_{Au}$[a] at different adsorbent doses (mg) | | | | | | average $S_{Au}$[a] | average $S_{Au}$[b] |
|---|---|---|---|---|---|---|---|---|---|
| | | 1 | 2 | 4 | 8 | 12 | 16 | | |
| $Fe_3O_4/SiO_2$/cPPyTh | Mg | 3.7766 | 4.92437 | 4.88585 | 4.79931 | 4.91492 | 5.04189 | 4.723823 | 52302.15742 |
| | Cu | 2.84828 | 4.58674 | 4.35398 | 4.43538 | 4.47631 | 4.41245 | 4.185523 | 15164.3552 |
| | Zn | 2.92823 | 4.73537 | 4.73954 | 4.82829 | 4.95081 | 5.07778 | 4.543337 | 34533.15306 |
| | As | –[c] | 4.92437 | 4.87102 | 4.94136 | 5.13299 | 5.25996 | 5.02594 | 104784.5902 |
| | Cd | – | – | – | 5.82284 | 5.93992 | 6.02904 | 5.9306 | 839347.43012 |
| | Pb | – | – | – | – | – | – | ∞ | ∞ |
| $Fe_3O_4/SiO_2$/PPy | Mg | 2.71361 | 3.40911 | 4.08034 | 3.80873 | 3.67766 | 3.68225 | 3.56195 | 3613.69112 |
| | Cu | 1.64929 | 2.42065 | 3.09034 | 3.12707 | 3.08749 | 3.12513 | 2.749995 | 558.35139 |
| | Zn | 2.05914 | 2.81459 | 3.42646 | 3.42813 | 3.44863 | 3.45343 | 3.105063 | 1263.50502 |
| | As | 3.45615 | 4.23137 | 3.84064 | 4.93856 | 5.05751 | 5.01424 | 4.423078 | 26188.59789 |
| | Cd | 1.92053 | 2.69575 | 3.30816 | 3.33578 | 3.34952 | 3.36425 | 2.995665 | 982.4304 |
| | Pb | 2.44308 | 3.14319 | 3.81442 | 3.85403 | 3.83067 | 3.87782 | 3.493868 | 3089.90739 |
| $Fe_3O_4/SiO_2$/PTh | Mg | 2.46838 | 2.16315 | 3.24058 | 4.50456 | 4.5498 | 4.61591 | 3.590397 | 3858.03436 |
| | Cu | – | – | – | 4.78113 | 4.60015 | 4.61996 | 4.66708 | 45902.91951 |
| | Zn | – | 1.97989 | 3.09426 | 4.50456 | 4.57847 | 4.63236 | 3.757908 | 5671.38367 |
| | As | 1.44621 | 1.61475 | 2.40386 | 3.8318 | 3.89212 | 3.93508 | 2.85397 | 709.19534 |
| | Cd | 1.46788 | 1.64101 | 2.73467 | 4.14063 | 4.24262 | 4.26399 | 3.0818 | 1197.67805 |
| | Pb | – | – | – | – | – | – | ∞ | ∞ |

a. The data derived from eq (3) in the text;[27] b. The data derived from eq of $S_{Au} = \frac{(Q_e/C_e)_{Au}}{(Q_e/C_e)_i}$, where *i* denotes the variety of interfering ions, $Q_e$ (mg $g^{-1}$) and $C_e$ (mg $L^{-1}$) correspond to the concentration of ions adsorbed upon the adsorbent and remnant in solution, respectively;[21] c. The "–" denotes an infinite $S_{Au}$ value.

## S13. Evidence for the formation of $Au^0$ upon the adsorbents

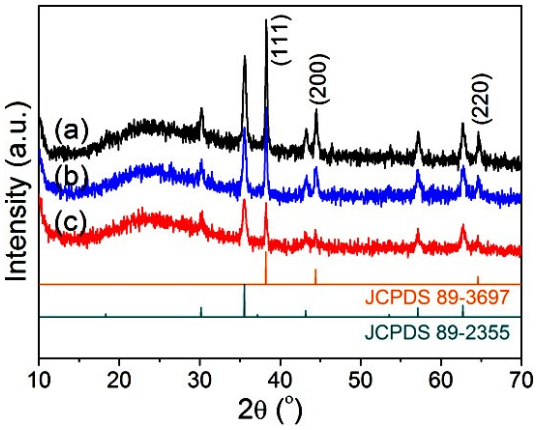


**Fig. S10** XRD spectra of the samples after adsorption of Au(III): (a) $Fe_3O_4/SiO_2$/cPPyTh; (b) $Fe_3O_4/SiO_2$/PPy; (c) $Fe_3O_4/SiO_2$/PTh.

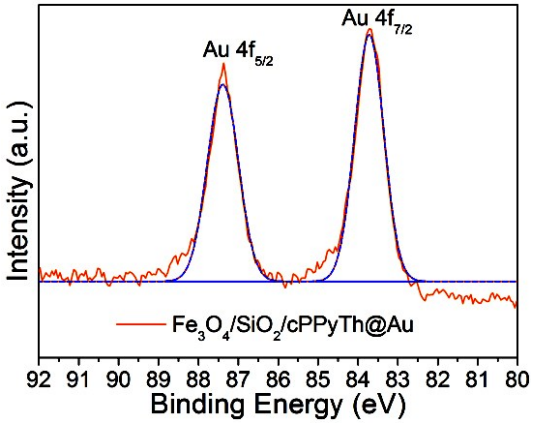


**Fig. S11** Au 4f spectrum of $Fe_3O_4/SiO_2$/cPPyTh@Au.

Fig. S10 shows the XRD spectra of the samples after Au(III) adsorption. After adsorption of Au(III), there are diffraction peaks corresponding to face-centered cubic Au (JCPDS 89-3697) aside from the diffraction peaks of $Fe_3O_4$ (JCPDS 89-2355). This result indicates an adsorption–reduction mechanism for Au(III) recovery.[28,29] Also, the mean size of Au nanocrystals on $Fe_3O_4/SiO_2$/cPPyTh,

$Fe_3O_4/SiO_2$/PPy, and $Fe_3O_4/SiO_2$/PTh is estimated to be 43, 31, and 50 nm, respectively, using the data of (111), (200), and (220) planes.

Fig. S11 shows the high-resolution Au 4f spectrum of $Fe_3O_4/SiO_2$/cPPyTh@Au. It exhibits two strong peaks at 83.7 and 87.4 eV, corresponding separately to Au $4f_{7/2}$ and Au $4f_{5/2}$ of $Au^0$,[30] in concert with the XRD result (Fig. S10).

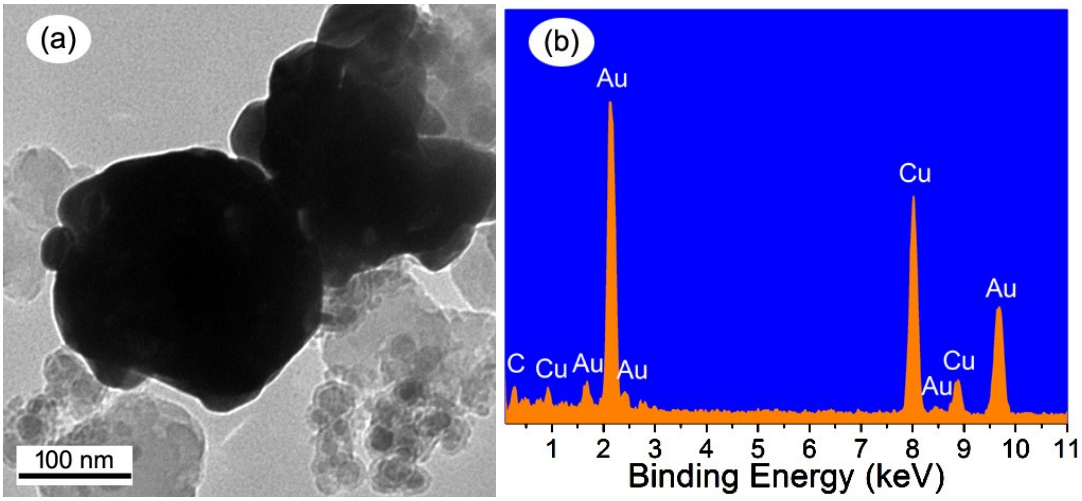


**Fig. S12** (a) TEM image of $Fe_3O_4/SiO_2$/cPPyTh@Au; (b) EDS pattern corresponding to the dark particles in a.

The existence of $Au^0$ can be differentiated from the adsorbent matrix. Au(0) tends to be densely packed to form gold nanoparticle aggregates with contrast in black (Fig. S12a). This is confirmed by the EDS pattern corresponding to the dark particles in Fig. S12a (Fig. S12b).

**References**

1 X. Peng, W. Zhang, L. Gai, H. Jiang, Y. Wang, L. Zhao, Dedoped $Fe_3O_4$/PPy nanocomposite with high anti-interfering ability for effective separation of Ag(I) from mixed metal-ion solution, Chem. Eng. J. 280 (2015) 197–205.

2 Y. Zhang, Q. Xu, S. Zhang, J. Liu, J. Zhou, H. Xu, H. Xiao, J. Li, Preparation of thiol-modified $Fe_3O_4$@$SiO_2$ nanoparticles and their application for gold recovery from dilute solution, Sep. Purif. Technol. 116 (2013) 391–397.

3 Y. Ren, H.A. Abbood, F. He, H. Peng, K. Huang, Magnetic EDTA-modified chitosan/$SiO_2$/$Fe_3O_4$ adsorbent: Preparation, characterization, and application in heavy metal adsorption, Chem. Eng. J. 226 (2013) 300–311.

4 P. Yin, M. Xu, W. Liu, R. Qu, X. Liu, Q. Xu, High efficient adsorption of gold ions onto the novel functional composite silica microspheres encapsulated by organophosphonated polystyrene, J. Ind. Eng. Chem. 20 (2014) 379–390.

5 A. Uygun, A. G. Yavuz, S. Sen, M. Omastová, Polythiophene/$SiO_2$ nanocomposites prepared in the presence of surfactants and their application to glucose biosensing, Synth. Met. 159 (2009) 2022–2028.

6 D.O. Kim, P.C. Lee, S.J. Kang, K. Jang, J.H. Lee, M.H. Cho, J.D. Nam, In-situ blends of polypyrrole/poly(3,4-ethylenedioxythiopene) using vapor phase polymerization technique, Thin Solid Films 517 (2009) 4156–4160.

7 M.B. Clark Jr., C.A. Burkhardt, J.A. Gardella Jr., Surface studies of polymer blends. 3. An ESCA, IR, and DSC study of poly(ε-caprolactone)/poly(vinyl chloride) homopolymer blends, Macromolecules 22 (1989) 4495–4501.

8 M. Wojnicki, E. Rudnik, M. Luty-Błocho, K. Pacławski, K. Fitzner, Kinetic studies of gold(III) chloride complex reduction and solid phase precipitation in acidic aqueous system using dimethylamine borane as reducing agent, Hydrometallurgy 127–128 (2012) 43–53.

9 Y.S. Ho, G. McKay, Sorption of dye from aqueous solution by peat, Chem. Eng. J. 70 (1998) 115–124.

10 R.J. Atkinson, F.J. Hingston, A.M. Posner, J.P. Quirk, Elovich equation for the kinetics of isotopic exchange reactions at solid–liquid interfaces, Nature 226 (1970) 148–149.

11 R.R. Sheha, A.A. El-Zahhar, Synthesis of some ferromagnetic composite resins and their metal removal characteristics in aqueous solutions, J. Hazard. Mater. 150 (2008) 795–803.

12 E. Raymundo-Pinero, K. Kierzek, J. Machnikowski, F. Béguin, Relationship between the nanoporous texture of activated carbons and their capacitance properties in different electrolytes, Carbon 44 (2006) 2498−2507.

13 L. Liu, S. Liu, Q. Zhang, C. Li, C. Bao, X. Liu, P. Xiao, Adsorption of Au(III), Pd(II), and Pt(IV) from Aqueous Solution onto Graphene Oxide, J. Chem. Eng. Data 58 (2013) 209−216.

14 Y.M. Hao, M. Chen, Z.B. Hu, Effective removal of Cu(II) ions from aqueous solution by amino-functionalized magnetic nanoparticles, J. Hazard. Mater. 184 (2010) 392–399.

15 M. Rossier, F.M. Koehler, E.K. Athanassiou, R.N. Grass, B. Aeschlimann, D. Günther, W.J. Stark, Gold adsorption on the carbon surface of C/Co nanoparticles allows magnetic extraction from extremely diluted aqueous solutions, J. Mater. Chem. 19 (2009) 8239–8243.

16 A. Kraus, K. Jainae, F. Unob, N. Sukpirom, Synthesis of MPTS-modified cobalt ferrite nanoparticles and their adsorption properties in relation to Au(III), J. Colloid Interface Sci. 338 (2009) 359–365.

17 M. Bayat, M.H. Beyki, F. Shemirani, One-step and biogenic synthesis of magnetic $Fe_3O_4$–Fir sawdust composite: application for selective preconcentration and determination of gold ions, J. Ind. Eng. Chem. 21 (2015) 912–919.

18 C. Sun, C. Li, C. Wang, R. Qu, Y. Niu, H. Geng, Comparison studies of adsorption properties for Hg(II) and Au(III) on polystyrene-supported bis-8-oxyquinoline-terminated open-chain crown ether, Chem. Eng. J. 200–202 (2012) 291–299.

19 C. Xiong, S. Zhou, X. Liu, Q. Jia, C. Ma, X. Zheng, 2-Aminothiazole functionalized polystyrene for selective removal of Au(III) in aqueous solutions, Ind. Eng. Chem. Res. 53 (2014) 2441−2448.

20 M. Fırlak, E.K. Yetimoğlu, M.V. Kahraman, Adsorption of Au(III) ions from aqueous solutions by thiol-ene photoclick hydrogels and its application to electronic waste and geothermal water, J. Water Process Eng. 3 (2014) 105–116.

21 Z. Dong, J. Liu, W. Yuan., Y. Yi, L. Zhao, Recovery of Au(III) by radiation synthesized aminomethyl pyridine functionalized adsorbents based on cellulose, Chem. Eng. J. 283 (2016) 504–513.

22 B. Pangeni, H. Paudyal, M. Abe, K. Inoue, H. Kavakita, K. Ohto, B.B. Adhikari, S. Alam, Selective recovery of gold using some cross-linked polysaccharide gels, Green Chem. 14 (2012)

1917–1927.

23 M. Bhaumik, A. Maity, V.V. Srinivasu, M.S. Onyango, Enhanced removal of Cr(VI) from aqueous solution using polypyrrole/$Fe_3O_4$ magnetic nanocomposite, J. Hazard. Mater. 190 (2011) 381–390.

24 Y.F. Pan, C.T. Chiou, T.F. Lin, Adsorption of arsenic(V) by iron-oxide-coated diatomite (IOCD). Environ. Sci. Pollut. Res. 17 (2010) 1401–1410.

25 V.C. Srivastava, I.D. Mall, I.M. Mishra, Adsorption thermodynamics and isosteric heat of adsorption of toxic metal ions onto bagasse fly ash (BFA) and rice husk ash (RHA), Chem. Eng. J. 132 (2007) 267–278.

26 Y. Wang, L. Gai, W. Ma, H. Jiang, X. Peng, L. Zhao, Ultrasound-assisted catalytic degradation of methyl orange with $Fe_3O_4$/polyaniline in near neutral solution, Ind. Eng. Chem. Res. 54 (2015) 2279–2289.

27 C. Xiong, S. Zhou, X. Liu, Q. Jia, C. Ma, X. Zheng, 2-Aminothiazole functionalized polystyrene for selective removal of Au(III) in aqueous solutions, *Ind. Eng. Chem. Res.*, 2014, **53**, 2441−2448.

28 F. Wang, J. Zhao, M. Zhu, J. Yu, Y.S. Hu, H. Liu, Selective adsorption–deposition of gold nanoparticles onto monodispersed hydrothermal carbon spherules: a reduction–deposition coupled mechanism, J. Mater. Chem. A 3 (2015) 1666–1674.

29 S.I. Park, I.S. Kwak, S.W. Won, Y.S. Yun, Glutaraldehyde-crosslinked chitosan beads for sorptive separation of Au(III) and Pd(II): Opening a way to design reduction-coupled selectivity-

tunable sorbents for separation of precious metals, J. Hazard. Mater. 248–249 (2013) 211–218.

30 J. Sundaramurthy, R. Dharmarajan, M.P. Srinivasan, Fabrication of molecular hybrid films of gold nanoparticle and polythiophene by covalent assembly, Thin Solid Films 589 (2015) 238–245.

31 A. Aydın, M. İmamoğlu, M. Gülfen, Separation and Recovery of Gold(III) From Base Metal Ions Using Melamine–Formaldehyde–Thiourea Chelating Resin, J. Appl. Polym. Sci. 107 (2008) 1201–1206.